



Design of PGM-free cathodic catalyst layers for advanced PEM fuel cells



Tatyana Reshetenko ^a, Madeleine Odgaard ^b, Günter Randolph ^c, Kenta K. Ohtaki ^d, John P. Bradley ^d, Barr Zulevi ^e, Xiang Lyu ^f, David A. Cullen ^g, Charl J. Jafta ^f, Alexey Serov ^{f,*,1}, Andrei Kulikovsky ^{h,*}

^a Hawaii Natural Energy Institute, University of Hawaii, Honolulu, HI 96822, USA

^b IRD Fuel Cells, LLC, 8500 Washington St. NE, Albuquerque, NM 87113, USA

^c GRandalytics, 2343 Oahu Avenue, Honolulu, HI 96822, USA

^d University of Hawaii, Advanced Electron Microscopy Center, Honolulu, HI 96822, USA

^e Pajarito Powder, LLC (PPC), Albuquerque, NM 87102, USA

^f Electrification and Energy Infrastructures Division, Oak Ridge National Laboratory, Oak Ridge, TN 37831, USA

^g Center for Nanophase Materials Sciences, Oak Ridge National Laboratory, Oak Ridge, TN 37831, USA

^h Forschungszentrum Jülich GmbH, Institute of Energy and Climate Research, IEK-13: Theory and Computation of Energy Materials, D-52425 Jülich, Germany

ARTICLE INFO

Keywords:
PEM fuel cell
PGM-free electrode
Proton conductivity
Electron conductivity
Impedance
Modeling

ABSTRACT

The design of cathodic catalysts layer (CCL) consisted of Platinum Group Metal-free (PGM-free) electrocatalysts was done by catalyst coated membrane approach. Three different Fe-Mn-N-C compounds were synthesized with Fe:Mn ratio of 1:1, 2:1 and 2:2 with modified heat treatment profile. The catalysts were characterized by X-ray photoelectron spectroscopy, X-ray powder diffraction, pore and particle size distribution, zeta potential and transmission electron microscopy. Electrocatalysts were integrated into membrane electrode assembly and evaluated by electrochemical methods. Electrochemical impedance spectroscopy in combination with modeling were used for estimation of proton conductivity of CCL and its oxygen diffusivity. It was found that all CCLs possess extremely high proton conductivity, which was demonstrated for the first time for these types of PGM-free catalysts. The observed ORR mechanism was predominantly 4e⁻ due to peroxide/radicals scavenging effect of Mn.

1. Introduction

The development of Platinum Group Metal-free (PGM-free) catalysts for cathodic Oxygen reduction reaction (ORR) in Polymer Exchange Membrane Fuel Cells (PEMFCs) resulted in substantial increase in intrinsic activity of these materials, their stability and in some cases durability [1–23]. As it is shown in majority of recent research papers the iron-based materials, generally abbreviated as Fe-N-C are the most promising for being used as a substitution of platinum from the cathodic side of membrane electrode assembly (MEA) [4,13,17]. It should be noticed, that interest to Fe-N-C ORR catalysts expanded from purely academic institutions to the industrial fuel cell manufacturers, and this demand is satisfied by commercial manufacturer of PGM-free catalysts US-based company Pajarito Powder, LLC [4,11,15].

Despite the improvement of ORR activity of catalysts themselves, their performance in the real fuel cell tests is still below that of Pt/C

materials [1,2,4,5]. That is mainly related to difficulties of integration Fe-N-C electrocatalysts into the cathodic catalyst layer (CCL), to achieve an efficient triple-phase boundary. Due to lower ORR activity, the PGM-free CCL has a thickness of ~100 μm in contrast to Pt/C-based CCL (5–10 μm), which makes the design of optimal oxygen diffusion, proton transport and water management an extremely difficult task. In order to make better electrodes with Fe-N-C catalysts knowledge on the factors affecting overall fuel cell performance is needed. We would like to refer the readers to the recent comprehensive reviews on the challenges and perspectives of the development of PGM-free ORR catalysts [24,25].

The most powerful tool for non-destructive in operando characterization of PEM fuel cells is electrochemical impedance spectroscopy [26,27] (see also a seminal paper by Macdonald with historical perspective of EIS [28]). Over the past decade, a number of publications on EIS in fuel cell studies exhibited exponential growth. Any transport or kinetic

* Corresponding authors.

E-mail addresses: serova@ornl.gov (A. Serov), a.kulikovsky@fz-juelich.de (A. Kulikovsky).

¹ Previously Affiliated with Pajarito Powder, LLC, USA.

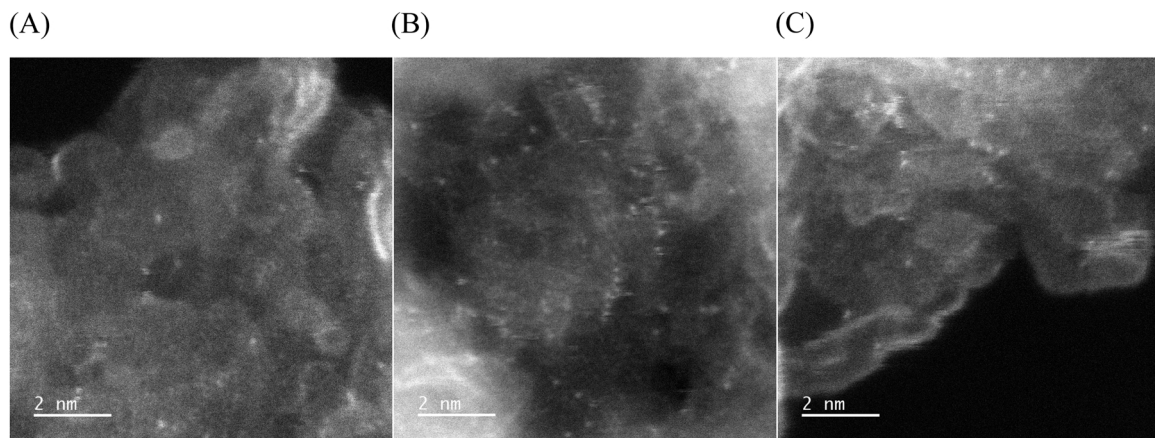


Fig. 1. High resolution TEM images of (A) Fe:Mn, (B) 2Fe:Mn and (C) 2Fe:MnT electrocatalysts.

process in the cell eventually changes proton and electron currents, thereby changing the cell impedance. In this way, impedance spectra contain information on transport and kinetic parameters of PEMFC's. However, retrieval of this information is a complicated task.

A pioneering work of Springer, Zawodzinski, Wilson and Gottesfeld [29] published in 1996 gave rise to development of analytical and numerical physics-based models for cell impedance [30–46]. (more references can be found in a recent review [47]). Models of that type are usually based on macroscopic transient mass and charge conservation equations in the cell. Fitting of model impedance to experimental spectra gives model parameters, e.g., diffusion coefficients of species participating in the charge-transfer reactions, kinetic rate constants etc.

The model employed in this work is based on macro-homogeneous transient oxygen and proton current conservation equations on the cathode side of the cell and it was successfully used in several studies on Pt/C-based PEMFCs [48–51]. With minor modifications, this model has been applied for characterization of PGM-free catalysts [15,52].

In this work we present comprehensive evaluation of three different bi-metallic compounds Fe-M-N-C were synthesized by hard-templating approach. It should be noticed that detailed mechanistic properties of Fe-M (including M=Mn) were previously studied by Rotating Ring Disk Electrode (RRDE) method and published by the authors [53]. The catalysts were integrated into the CCL using proprietary spraying method practiced by industrial MEAs manufacturer IRD Fuel Cells. The electrochemical evaluation of MEAs, including EIS with modeling were used to obtain and analyze such crucial for fuel cell performance parameters as oxygen diffusivity, proton conductivity, Tafel parameter and contribution to an ORR $4e^-$ and $2e^-$ mechanism.

2. Experimental

2.1. Catalysts synthesis

The synthesis of Fe-N-C materials can be found in detail in our previously published works [15,54]. Three electrocatalysts were prepared with various Fe:Mn ratio: 1) Fe:Mn = 1:1 (Sample: Fe:Mn), 2) Fe:Mn = 2:1 (Samples: 2Fe:Mn and 2Fe:MnT (treated at different heat temperature profile)). The iron and manganese nitrates, nicarbazin and silica were dispersed in water until viscous paste was made. The mixture was dried at $T = 85^\circ\text{C}$ for 8 h and heat treated in the atmosphere of N_2 at $T = 950^\circ\text{C}$ for 90 min (all three samples). The silica was removed by soaking powder in 25 wt% of HF for 24 h and Fe-N-C material was washed with water until $\text{pH} = 6$. The second heat treatment was done in N_2 atmosphere at $T = 1000^\circ\text{C}$ for 45 min (Fe:Mn and 2Fe:Mn); $T = 1050^\circ\text{C}$ for 45 min (2Fe:MnT) and powders were used for MEA preparation.

2.2. MEA preparation

Catalyst coated membranes (CCMs) were manufactured by IRD Fuel Cells, LLC using a trademarked membrane material and a digital spray coating method. Pt/C catalyst was used for an anode electrode with loading of $0.2 \text{ mg}_{\text{Pt}} \text{ cm}^{-2}$. The PGM-free catalyst loading at a cathode was 2.0 and 3.0 mg cm^{-2} . To distinguish the samples, we included the catalyst loading to the MEA abbreviation. For example, "Fe:Mn-2.0" means MEA with Fe:Mn catalysts and 2.0 mg cm^{-2} loading etc. The MEAs were fabricated by hot-pressing a CCM, gas diffusion layers (GDLs) and gaskets at 140°C and 2000 lbs of force pressure for 4 min. Freudenberg H23C8 GDLs with thickness of $220 \mu\text{m}$ were applied for both electrodes. The gasket material thickness was 155 and $255 \mu\text{m}$ for the anode and cathode, respectively, to provide compression ratio of 20%.

2.3. Fuel cell testing

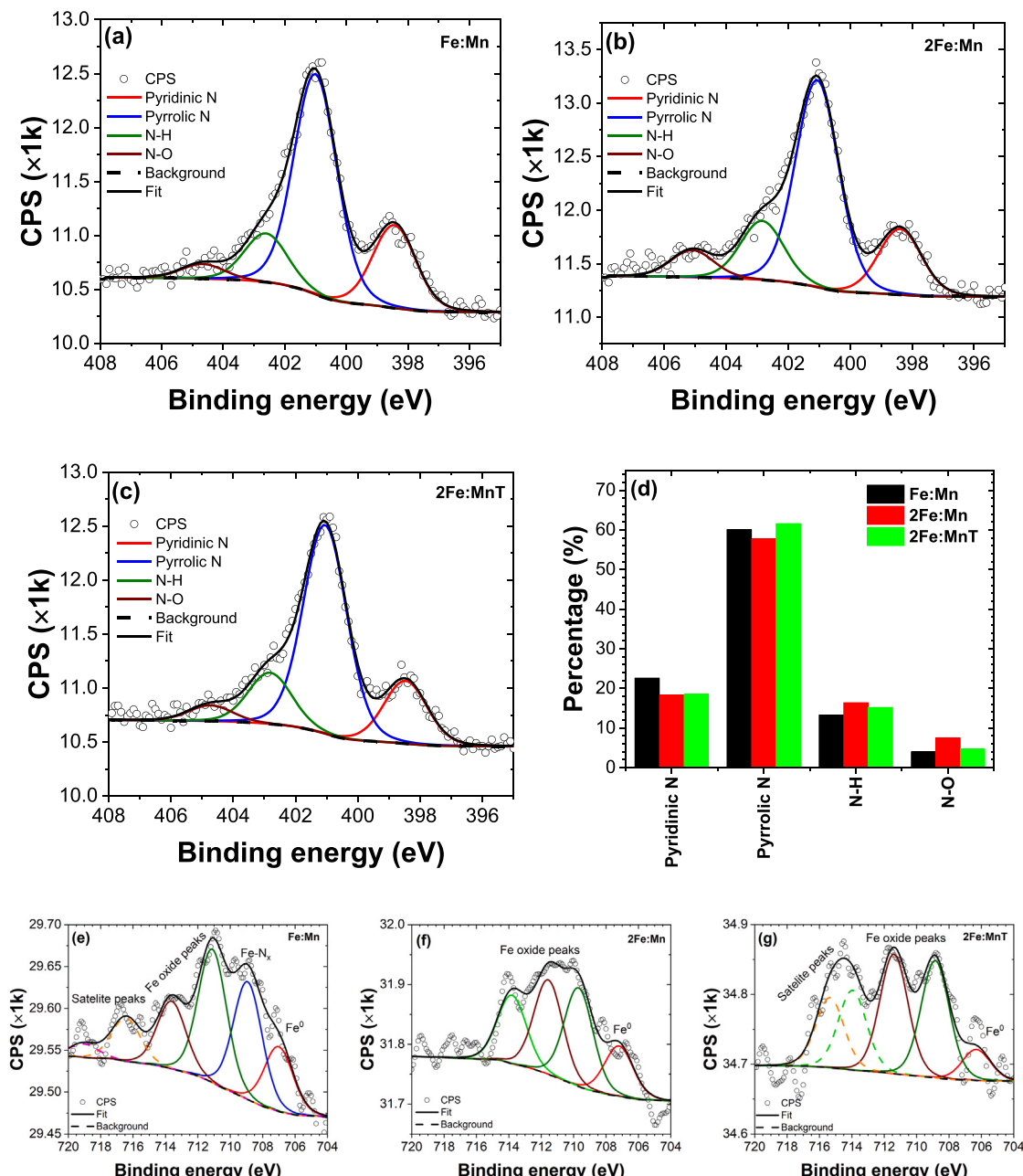
Electrochemical testing of PGM-free MEAs were performed using a test station, custom-built at the Hawaii Natural Energy Institute, and characterized by dynamic response time $< 0.1 \text{ s}$. MEAs evaluation was carried out using a cell hardware manufactured by Fuel Cell Technology Inc. Anode and cathode flow fields had triple serpentine design. Polarization curves measurements were performed under potentiostatic control of load. Cell was operated at a temperature of 80°C , 100% relative humidity and 150 kPa absolute backpressure for both electrodes. The anode and cathode were fed with H_2 and O_2 respectively, at constant flow rates of 0.51 min^{-1} for all range of applied potentials. The testing protocol included recording five IV curves from ocv to 0.6 V and additional three curves from ocv to 0.2 V. All polarization curves were run in forward and backward directions. High-frequency resistance was measured simultaneously with IV using an integrated proprietary multichannel impedance module as one-point impedance response at 1 kHz frequency. EIS measurements were performed under galvanostatic control of the cell current and at 11 steps/decade. The selected frequency range for the EIS experiments was 0.1 Hz to 10 kHz and the amplitude of sinusoidal current signal corresponded to a cell voltage perturbation of 10 mV or lower to ensure that the measured impedance response satisfies linearity condition.

Details on physical-chemical characterization of catalysts and CCL as well as description of the EIS model used in this work are presented in [Supplementary information](#).

Table 1

Summary of morphological data on catalyst powders.

Sample	Surface area, $\text{m}^2 \text{ g}^{-1}$	Prominent pore diameter, nm	Pore volume, cm^3	Average particle size, nm	Crystallite size (XRD), nm	Number of graphene layers (XRD), a. u.
Fe:Mn	1200	10	1.00	340	4.3	20
2Fe:Mn	1300	7.5	1.30	410	3.5	19
2Fe:MnT	1400	7	1.4	410	2.7	16

**Fig. 2.** The N 1s detailed XPS spectra from samples (a) Fe:Mn, (b) 2Fe:Mn, and (c) 2Fe:MnT with (d) showing the content of the different N species in each sample as a percentage. The Fe 2p detailed spectra from samples (e) Fe:Mn, (f) 2Fe:Mn, and (g) 2Fe:MnT.

3. Results and discussion

3.1. Electrocatalysts characterization

The synthesized electrocatalysts were comprehensively characterized in order to establish their morphology, presence or absence of

unreacted iron or manganese compounds and chemical composition. High angle annular dark-field (HAADF) images of all three catalysts, acquired using aberration-corrected scanning transmission electron microscopy, are shown on Fig. 1. The graphitized carbon matrix hosts atomically dispersed transition metals atoms (bright spots). Energy-dispersive X-Ray spectroscopy (EDX) of these catalysts showed the

Table 2

Summary on chemical composition, Zeta-potential and pH on catalyst powders.

Sample	C, at %	O, at %	N, at %	Mn, at%	Fe, at%	Zeta-potential, mV	Immersed pH
Fe:Mn	98.23	1.47	0.25	0.04	0.01	33.0	6.1
2Fe:Mn	98.46	1.23	0.28	0.02	0.02	25.8	7.2
2Fe: MnT	98.47	1.35	0.15	0.02	0.01	16.4	5.6

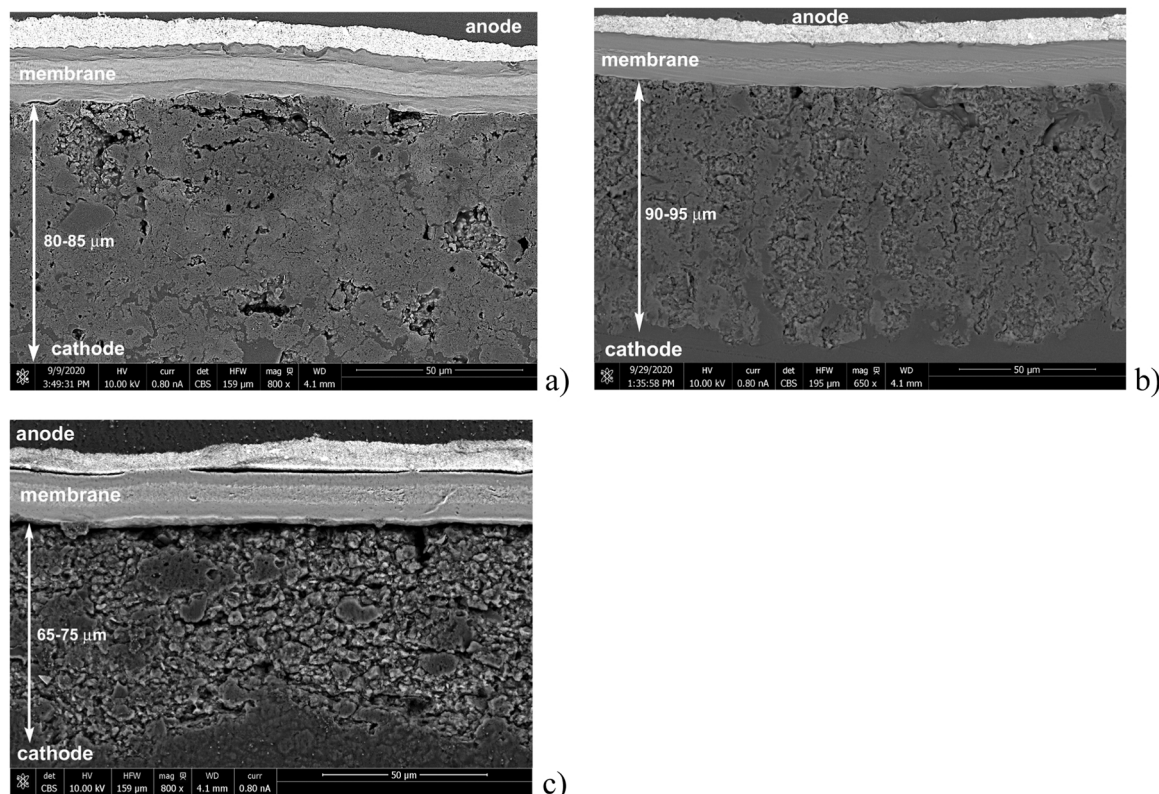
presence of both Mn and Fe in the catalyst powder. Single-atom electron energy loss spectroscopy (EELS) can be used to probe the composition of individual transition metal atoms and their neighboring environment. However, it is well known that the low-voltage beam can dislodge the transition metal atom in the few seconds it takes to collect a spectrum with sufficient signal-to-noise ratio for precise elemental quantification [55]. Interestingly, it was observed in the course of acquisition of single-atom EEL spectra that manganese single atoms were much more likely to be detected than iron, which suggests increased durability of the Mn site against demetallation [56] which suggests increased durability of the Mn site against demetallation.

Besides TEM, morphology was studied by nitrogen isotherm pore size analysis (surface area, pore size distribution (PSD) and pore volume), Dynamic Light Scattering method (particle size distribution: includes aggregates and agglomerates of particles) and XRD (crystallite size and number of graphene layers in the catalysts) (Figs. S2, S3). The data were summarized in Table 1.

It was found that hard template method in combination with selected heat treatment parameters resulted in materials with high surface area (SA) and large pore volume. Sample 2Fe:MnT had a largest surface area of $1400 \text{ m}^2 \text{ g}^{-1}$ and pore volume of 1.4 cm^3 . PSD, crystallite size and number of graphene layers in a structure of this catalysts were smallest in a set of three Fe-Mn-N-C materials. Such a combination should result in formation of larger area where single atomic active sites can be

located [57].

The surface chemical composition and speciation is extremely important for electrocatalysis, and in many cases can be correlated with electrochemical performance [58]. All bi-metallic catalysts were evaluated using XPS in order to understand which surface chemical moieties are present in the carbon matrix (Fig. 2). As described in the Experimental section, in order to remove the hard template (fumed silica) and the unreacted iron/manganese compounds, the catalysts were extensively washed in a mixture of nitric and hydrofluoric acids. This resulted in the elimination of all accessible metallic compounds (metal nanoparticles, carbides, nitrides, oxides and mixed compounds) leaving only atomically dispersed active sites. This is confirmed by a combination of XRD, TEM and XPS measurements. As a result, due to the low Fe and Mn concentrations, the XPS signals for these elements resulted in low signal-to-noise ratio spectra which cannot unambiguously be used for metallic quantitative analysis. It is however possible to conclude that the Fe and Mn content in the catalysts are within the limits of XPS, which is in the order of 0.1 at%. Indeed, based on the TEM EDX data the concentration of Fe and Mn was in the order of 0.05 at% (Table 2), which is lower compared to monometallic Fe-N-C compounds [4]. This result could also be an indication of the increased surface concentration of Fe and Mn as compared to the bulk concentrations. As shown by Artyushkova et. al. [58] the different types of nitrogen and its concentrations play a critical role in ORR. From the XPS spectra, all three catalysts consist of pyridinic N (398.4 eV), pyrrolic N (401.1 eV), N-H (402.9 eV) and N-O (405.1 eV) [58,59]. Further analysis of the N1s spectra shows that the Pyrrolic N is the most prominent for all the catalysts followed by Pyridinic N, N-H and N-O (Fig. 2d). The fitted pyrrolic N peak for the Fe: Mn catalyst has a slightly lower binding energy (401.0 eV) as compared to the other catalysts, that is within the energy resolution error of the measurement (0.1 eV), however, this could be an indication of a metal (M)-N bond [58,60]. In order to confirm the M-N bond, the Fe 2p spectra (Fig. 2e-g) was treated, as per the report by Artyushkova et al. [58], where it was smoothed (Gaussian function in this case) and fitted. It is

**Fig. 3.** SEM images of the samples: Fe:Mn-2.0 (a), 2Fe:Mn-2.0 (b) and 2Fe:MnT-2.0 (c).

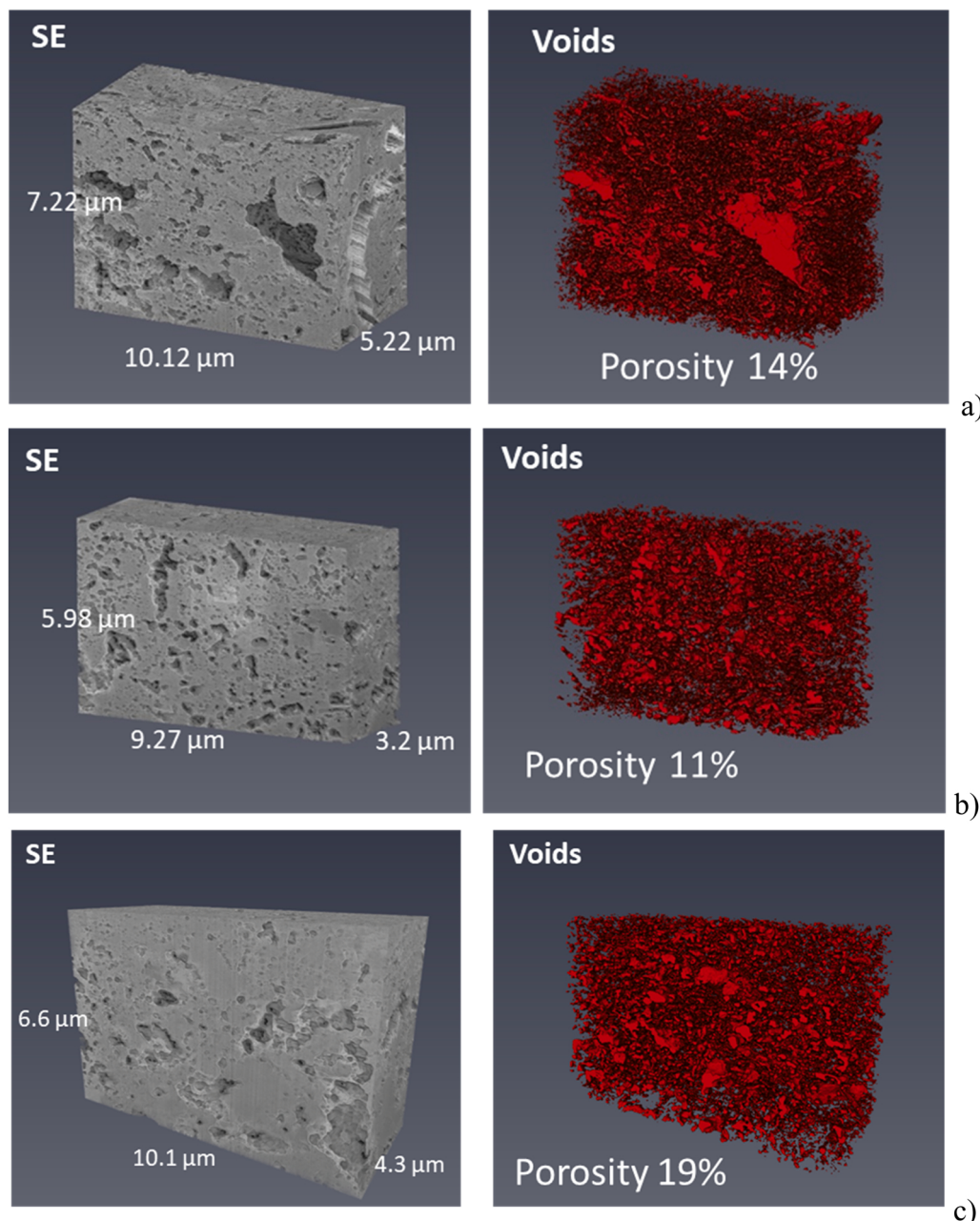


Fig. 4. 3D reconstruction images (SE and voids) and void diameter distributions for Fe:Mn-2.0 (a), Fe:2Mn-2.0 (b) and Fe:2MnT-2.0 (c).

clearly observed that all the samples have a peak at ≈ 707 eV indicating metallic Fe and different Fe oxide peaks between ~ 710 and 714 eV, however only the Fe:Mn sample has a distinct peak at ≈ 708 eV that is due to a Fe- N_x bond, corroborating the M-N bond indicated by the N 1s spectrum. From the Mn 2p spectra in Fig. S4, it is observed that the peaks are at the same binding energy positions, for all three samples, and thus the Mn oxidation states are assumed to be the same. The catalyst with the highest pyridinic N is Fe:Mn which is shown to have higher activity towards oxygen reduction. The same catalyst has the lowest amount of nitrogen atoms bonded to hydrogen and oxygen, having the N accessible for oxygen adsorption during ORR [61]. Fig. 2 shows the XPS N1s detailed spectra from samples Fe:Mn, Fe:2Mn, and Fe:2MnT, with all the samples having N components.

Interestingly, while the exact bulk ratio between Fe and Mn was not preserved in final catalysts, systematically samples with Fe:Mn = 2:1 showed higher ratio of Fe to Mn (Table 2). Stabilization of transition metals in the carbon matrix requires that the atomically dispersed metal

centers be coordinated with nitrogen forming M- N_x center. In this case Mn and Fe are competing for such coordination. It can be hypothesized that material with lower Mn content should have a higher catalytic activity, as was confirmed by electrochemical evaluation discussed below. On the other side, as it was shown previously addition of manganese substantially decreases amount of hydrogen peroxide formation, which should improve durability of catalyst Fe-Mn with highest Mn content. This observation is confirmed by recent publications on single Mn-N-C catalysts [62,63].

3.2. Cathodic catalysts layers characterization

Fully characterized electrocatalysts were integrated into the CCM structures using a proprietary spray coating method developed by industrial MEA manufacturer IRD Fuel Cells. The cross-section of such CCMs with catalyst loading of 2.0 mg cm^{-2} is shown on Fig. 3. The obtained SEM data clearly revealed grains with different contrast in the

Table 3

Summary of physical-chemical data of CCLs.

Sample	Thickness, μm	Porosity level, %	Voids diameter, nm	Contact angle, $^\circ$
Fe:Mn-2.0	80–85	14	30–45	170
Fe:2Mn-2.0	90–95	11	25–45	172
Fe:2MnT-2.0	65–75	19	25–60	173

electrode structures with size from several to 20 μm . These formations could be attributed to catalyst agglomerates with primary pores of ~ 10 –50 nm inherited from internal porosity in initial carbon structures. These catalyst agglomerates seem to bound together with ionomer and develop macroscopic structures with secondary pores up to 1 μm . This advanced porous network penetrates the thick catalyst layers of 65–95 μm .

CCL of Fe:Mn was found to be quite dense while samples 2Fe:Mn and 2Fe:MnT demonstrated structures with formed channels coming from membrane towards microporous layer (MPL) of GDL. This direction coincided with water repelling pathway during the ORR, when majority of water formed in triple-phase boundary close to membrane. Water flooding of CCL is one of the possible mechanisms of the PGM-free catalysts activity degradation. Having less dense structure with channels may help water mass-transport and decrease the flooding of active sites.

Additional analysis of cathodic catalyst structures was done using Focus Ion Beam (FIB) SEM method (Fig. 4). Several random selected slabs of CCL were used for obtaining images followed by features reconstructions. As it can be seen on Fig. 4 the trend in density and porosity level fully agrees with data obtained by cross-section SEM discussed above. The highest level of porosity was attributed to the sample Fe:2MnT achieving about 20%. Average void diameter was estimated to be 25–35 nm for all samples. Higher level porosity and

irregular channels in the CCM related sample 2Fe:MnT can be explained by lowest zeta-potential of this sample (Table 2). Lower values of zeta-potential pointed out on less stable colloidal inks for coatings, which may lead to less dense structures, due to faster agglomeration of the particles. An important for cathodic catalyst layer parameter – level of hydrophobicity was estimated by using contact angle measurement technique (Table 3 and Fig. S5). Contact angles for all three samples were found to approximately the same and achieved extreme values of $\sim 170^\circ$ and higher.

Such value makes all three CCM super hydrophobic, which improves water removal from the whole CCL and preventing water flooding.

3.3. Electrochemical characterization and EIS modeling

Fig. 5 presents IV curves recorded for samples with 2.0 and 3.0 mg cm^{-2} catalyst loadings. The initial OCV of all MEAs were in the range of 0.921–0.948 V. The IV #1 showed that 2Fe:MnT-2.0 sample had the best performance for series with 2.0 mg cm^{-2} catalyst loading (Fig. 6 a). An increase in the cathode content to 3.0 mg cm^{-2} improved performance of Fe:Mn-3.0 and kept high performance of 2Fe:MnT-3.0 (Fig. 6 b). However, continuous repeating polarization curves in forward and backward directions led to degradation of the catalysts as can be seen from Fig. 5 c and d. Interestingly, the resulting performance of the MEAs within one series of the cathode loadings was found to be close after eight polarization curves. Values of current density at fixed potential as of measured polarization curve are demonstrated at Fig. S6. The results clearly reveal the dynamic of the degradation and confirmed that 2Fe:MnT is the best catalyst among 2.0 and 3.0 mg cm^{-2} loadings.

Experimental and fitted model Nyquist curves and Bode plots are presented at Figs. 6 and S7. All samples had the close high-frequency (HFR) values in the range of 40–80 mOhm cm^2 depending on operating current. All impedance curves obtained at 50–100 mA cm^{-2} have clearly distinguished 45° slope at high frequency slope indicating on uniform proton conductivity of our cathodes. The impedance spectra

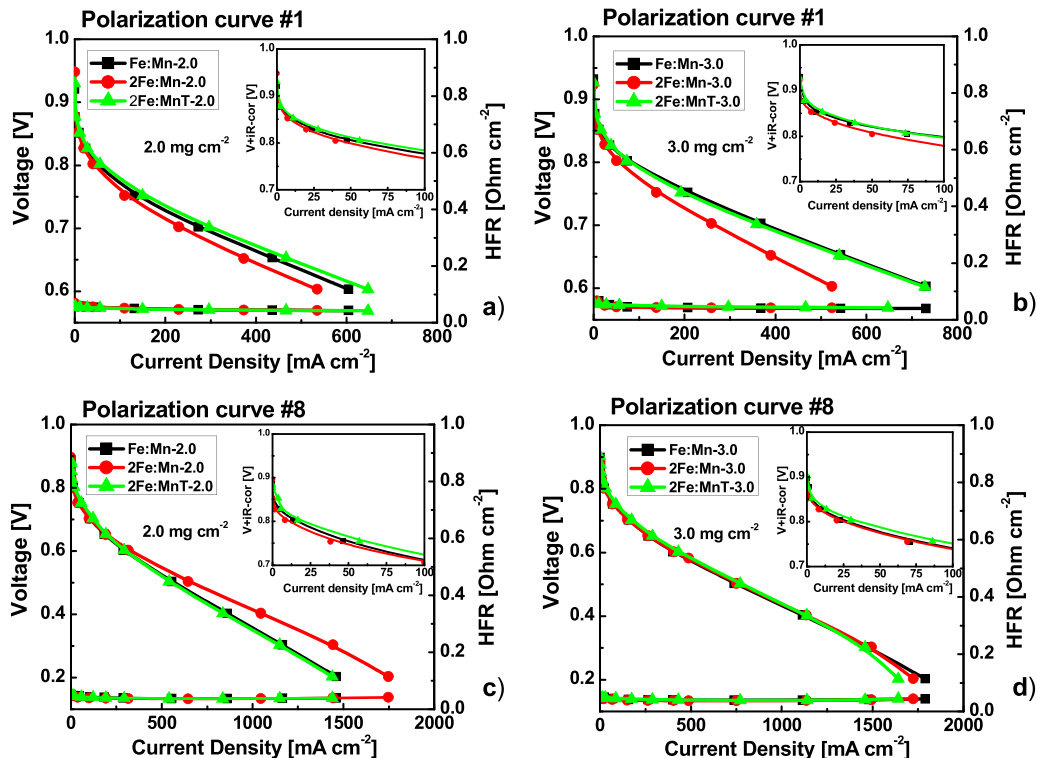


Fig. 5. Polarization curves for the studied samples: a) IV curves #1 for MEAs with Fe-N-C catalyst loading of 2.0 mg cm^{-2} , b) IV curves #1 for MEAs with Fe-N-C catalyst loading of 3.0 mg cm^{-2} , c) IV curves #8 for MEAs with Fe-N-C catalyst loading of 2.0 mg cm^{-2} , d) IV curves #8 for MEAs with Fe-N-C catalyst loading of 3.0 mg cm^{-2} . An/Ca: H_2/O_2 , 0.5/0.5 1min^{-1} , 100/100%RH, 150 kPa and 80 $^\circ\text{C}$.

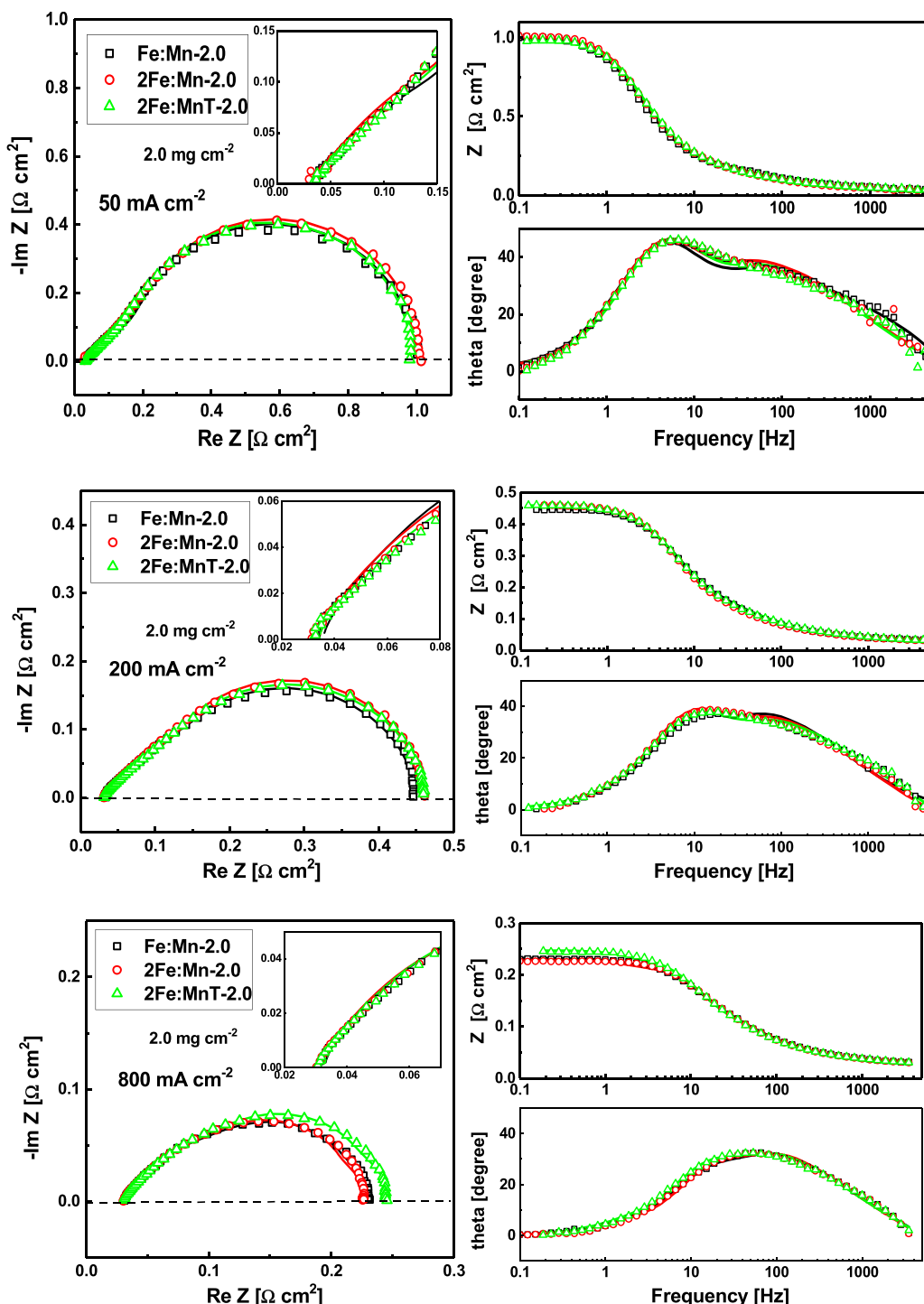


Fig. 6. Nyquist spectra and Bode plots for samples with catalyst loading of 2.0 mg cm^{-2} recorded at different currents. Experimental (points) and fitted model (solid line). An/Ca: H_2/O_2 , $0.5/0.5 \text{ l min}^{-1}$, 100/100%RH, 150 kPa and 80°C .

showed one depressed semi-circle attributed to charge transfer resistance and double layer capacitance due to ORR on PGM-free catalysts. Operation with pure O_2 eliminated any possible mass transport impedance. Our data showed that EIS curves for all MEAs within the appropriate cathode loading series are very close.

The parameters of the samples resulted from spectra fitting are shown in Fig. 7. The ORR Tafel slope in all the three cells was nearly the same and it increased with the cell current up to 250 mV per decade. The CCL proton conductivity also exhibited a moderate growth from 20 mS cm^{-1} at 50 mA cm^{-2} up to 40 mS cm^{-1} at 1 A cm^{-2} . The growth

of the CCL proton conductivity (σ_p) can be attributed to accumulation of liquid water in the CCL; water may also contribute to the growth of Tafel slope. The volumetric double layer capacitance was around 10 F cm^{-3} and it practically did not change with the cell current. The CCL oxygen diffusivity (D_{O_2}) demonstrated rapid linear growth in the range of cell currents 50 – 400 mA cm^{-2} , followed by the explosive growth up to undetectable high value. In [15], the cells exhibited much lower proton conductivity and estimates showed that the ORR rate had a distinct peak at the membrane surface. This peak suggested that the explosive growth of D_{O_2} could be due to formation of temperature and pressure gradients

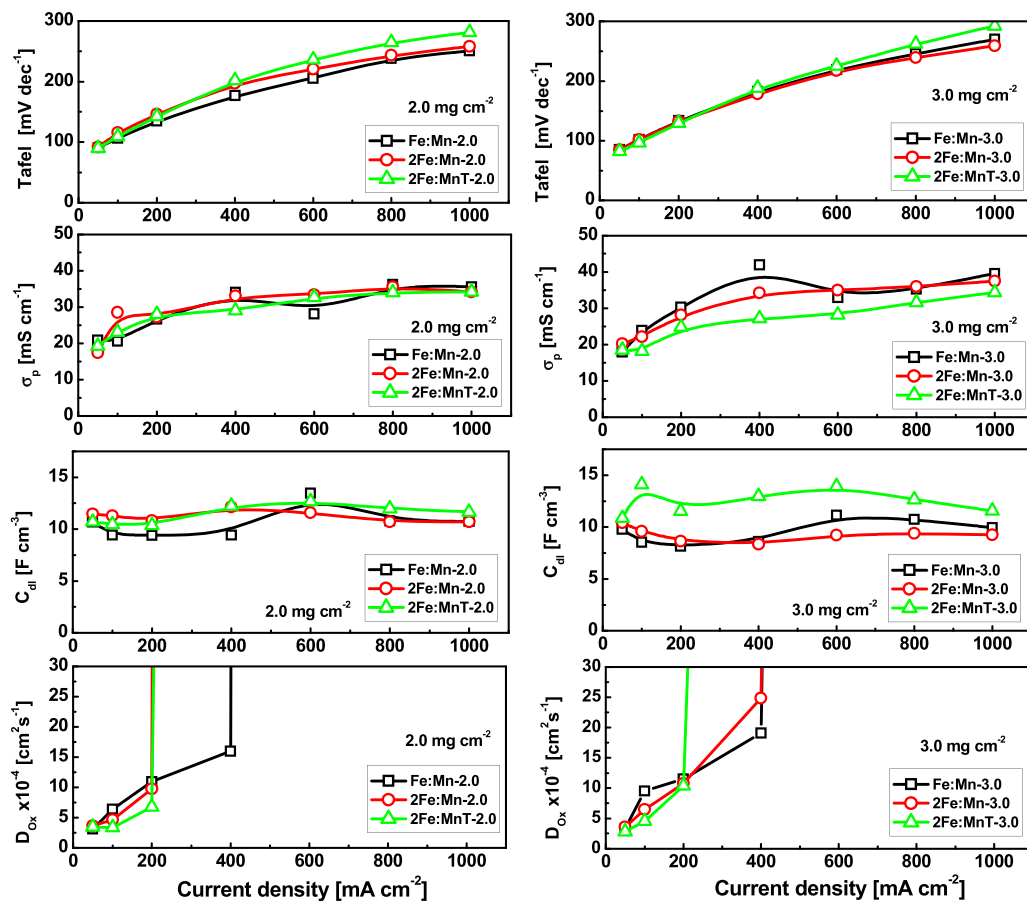


Fig. 7. ORR Tafel slope, CCL proton conductivity, double layer volumetric capacitance, and oxygen diffusivity.

Table 4

Electrochemical performance and catalyst layer properties: Tafel, proton conductivity (σ_p) double layer capacitance (C_{dl}), oxygen diffusivity in CCL (D_{Ox}) and fraction of 2 e⁻ ORR pathway ($fj2e$).

Sample	ocv, V	$i@0.8$ V, mA cm^{-2}	Tafel@50 mA cm^{-2} , mV/dec	$\sigma_p@600$ mA cm^{-2} , mS cm^{-1}	$C_{dl}@600$ mA cm^{-2} , F cm^{-3}	$D_{Ox} \times 10^4$ @200 mA cm^{-2} , $\text{cm}^2 \text{s}^{-1}$	$fj2e@600$ mA cm^{-2}
Fe:Mn-2.0	0.921	58	91	28.1	13.5	10.9	$2 \cdot 10^{-2}$
2Fe:Mn-2.0	0.948	49	92	33.4	11.6	9.8	$4 \cdot 10^{-4}$
2Fe:MnT-2.0	0.930	69	90	32.6	12.7	6.8	$9 \cdot 10^{-3}$
Fe:Mn-3.0	0.932	90	85	32.9	11.1	11.5	$2 \cdot 10^{-4}$
2Fe:Mn-3.0	0.923	62	85	34.9	9.2	10.8	$3 \cdot 10^{-3}$
2Fe:MnT-3.0	0.927	92	82	28.2	13.9	10.4	$6 \cdot 10^{-6}$

facilitating liquid water removal from the CCL.

Here, the CCL proton conductivity was nearly four times higher than in [15], meaning much more uniform distribution of the ORR rate through the CCL depth. Such significant improvement of the proton conductivity can be due to several factors: reduced loading of the PGM-free catalyst (it should be noted that loading was 2 and 3 mg cm^{-2} , which is significantly lower a standard loading of 4–8 mg cm^{-2}) and due to decreased size of particle agglomerates, see Table 1. Later should result in more uniform coating of the carbon particles with ionomer, resulting in decreased a proton pathway to the triple-phase boundary. Due to pure oxygen feed, the model may fail to correctly capture the contribution of oxygen transport to the cell impedance at higher currents, yielding “infinite” value of D_{Ox} . Overall, the effect of D_{Ox} growth with the cell current deserves further studies. Table 4 summarizes electrochemical performance data for the studied MEAs.

Fig. 8 shows the fraction $fj2e$ of total current density due to the two-electron ORR channel with H_2O_2 formation. This fraction has been calculated as (cf. Eq. Supplementary information (A2))

$$fj2e = \frac{1}{J} \int_0^{I_f} (1 - \beta) i_* \left(\frac{c^0}{c_h^{in}} \right) \exp \left(\frac{\eta_2^0}{b_a} \right) dx \quad (8)$$

where J is the mean cell current density.

At low cell currents, when the cell potential was above the 2e⁻ ORR threshold of 0.7 V, parameter $fj2e$ was negligibly small (Fig. 8). However, at the cell potentials below 0.7 V, the 2e⁻ overpotential became positive and the fraction of 2e⁻ ORR channel in the total cell current increased (Fig. 8). The curves demonstrated rather irregular dependence of $fj2e$ on the cell current density with the highest value of about 2% in the cell Fe:Mn-2.0 at the current of 600 mA cm^{-2} . This value was

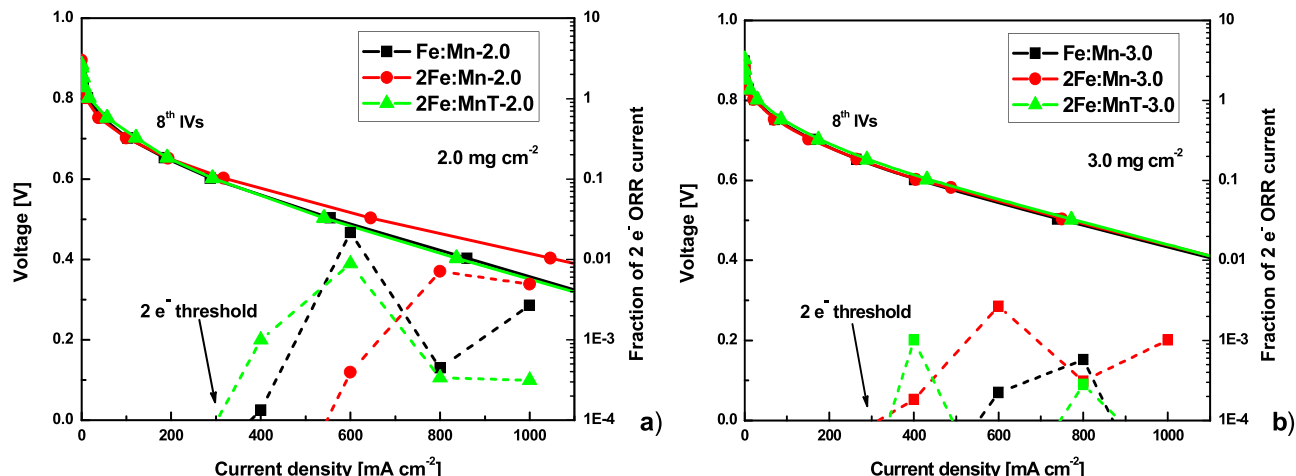


Fig. 8. Fraction of $2e^-$ ORR channel in the mean cell current density for the MEAs with 2.0 (a) and 3.0 mg cm^{-2} (b) catalyst loadings. The first and the last (8th) IV curves presented for comparison.

equivalent to the H_2O_2 flux of 12 mA cm^{-2} in electric units. At other current densities and in the other cells, the H_2O_2 flux was one to two orders of magnitude lower, not exceeding 1 mA cm^{-2} . The obtained data clearly showed that bi-metallic Fe-Mn-N-C electrocatalysts integrated in the MEAs ensured predominantly $4e^-$ ORR pathway which together with advanced electrode textural and structural properties improved overall MEAs performance.

4. Conclusions

The set of bi-metallic Fe-Mn electrocatalysts was synthesized by scalable hard templating method. Detailed characterization of these materials revealed that different ratio between iron and manganese, as well as temperature of synthesis effected catalysts morphology and chemical structure. Notably the materials described in present work have transition metals amounts (Fe and Mn) that are nearly an order of magnitude less than other M-N-C type catalysts previously reported, with similar performance in the cathodes of low temperature PEMFC. This can be indirect indication that intrinsic activity of these active sites can be substantially higher than previously reported and that the highly porous open-framed 3D structures in catalysts made by hard template method enabled exposure of Fe-N_x active sites to oxygen, improving activity in ORR. Materials with higher surface area and smaller pore sizes had higher activity, suggesting that the majority of active site are associated with defected structure of C-N matrix and pore sizes below 2 nm. MEAs with Fe-Mn-N-C electrocatalysts possess exceptional proton conductivity and oxygen permeability, which gives another tool for improving overall performance of PGM-free PEMFCs even with highly loaded and thick cathodes. Based on the results of EIS modeling the contribution of $2e^-$ ORR mechanism is negligible, which can be explained by excellent peroxide/radicals properties of manganese.

CRediT authorship contribution statement

Tatyana Reshetenko: Conceptualization, Methodology, Writing – original draft, Writing – review & editing. **Madeleine Odgaard:** Conceptualization. **Günter Randolph:** Methodology. **Kenta K. Ohtaki:** Methodology. **John P. Bradley:** Methodology. **Barr Zulevi:** Resources. **Xiang Lyu:** Methodology, Writing – original draft, Writing – review & editing. **David A. Cullen:** Methodology. **Charl J. Jafta:** Methodology, Writing – original draft, Writing – review & editing. **Alexey Serov:** Conceptualization, Supervision, Methodology, Writing – original draft, Writing – review & editing, Project administration. **Andrei Kulikovsky:** Conceptualization, Methodology, Writing – original draft, Writing – review & editing.

Declaration of Competing Interest

The authors declare that they have no known competing financial interests or personal relationships that could have appeared to influence the work reported in this paper.

Acknowledgment

TR gratefully acknowledges funding from US Office of Naval Research (N00014-18-1-2127, N00014-19-1-2159). MO, BZ, AS and TR gratefully acknowledge financial support from U.S. Department of Energy's Office of Energy Efficiency and Renewable Energy (EERE) under the Hydrogen and Fuel Cells Technologies Office (HFTO), FY2018 Hydrogen and Fuel Cell R&D FOA, Award no. DE-EE0008419. AS gratefully acknowledge financial support from the Oak Ridge National Laboratory SEED 10609 project "Single-Atom Catalysts for CO_2 Conversion". Aberration-corrected STEM was conducted at the Center for Nanophase Materials Sciences, which is a DOE Office of Science User Facility.

Appendix A. Supporting information

Supplementary data associated with this article can be found in the online version at [doi:10.1016/j.apcatb.2022.121424](https://doi.org/10.1016/j.apcatb.2022.121424).

References

- [1] S. Kabir, S. Medina, G. Wang, G. Bender, S. Pylypenko, K.C. Neyerlin, Improving the bulk gas transport of Fe-NC platinum group metal-free nanofiber electrodes via electrospinning for fuel cell applications, *Nano Energy* 73 (2020), 104791.
- [2] L. Osmieri, D.A. Cullen, H.T. Chung, R.K. Ahluwalia, K. Neyerlin, Durability evaluation of a Fe-N-C catalyst in polymer electrolyte fuel cell environment via accelerated stress tests, *Nano Energy* 78 (2020), 105209.
- [3] L. Osmieri, S. Mauger, M. Ulsh, K.C. Neyerlin, G. Bender, Use of a segmented cell for the combinatorial development of platinum group metal-free electrodes for polymer electrolyte fuel cells, *J. Power Sources* 452 (2020), 227829.
- [4] L. Osmieri, J. Park, D.A. Cullen, P. Zelenay, D.J. Myers, K.C. Neyerlin, Status and challenges for the application of platinum group metal-free catalysts in proton-exchange membrane fuel cells, *Curr. Opin. Electrochem.* 25 (2021), 100627.
- [5] L. Osmieri, G. Wang, F.C. Cetinbas, S. Khandavalli, J. Park, S. Medina, S.A. Mauger, M. Ulsh, S. Pylypenko, D.J. Myers, Utilizing ink composition to tune bulk-electrode gas transport, performance, and operational robustness for a Fe-N-C catalyst in polymer electrolyte fuel cell, *Nano Energy* 75 (2020), 104943.
- [6] L. Jiao, J. Li, L.L. Richard, Q. Sun, T. Stracensky, E. Liu, M.T. Sougrati, Z. Zhao, F. Yang, S. Zhong, Chemical vapour deposition of Fe-N-C oxygen reduction catalysts with full utilization of dense Fe-N4 sites, *Nat. Mater.* 20 (2021) 1385–1391.
- [7] M.R. Karim, M. Ferrandon, S. Medina, E. Sture, N. Kariuki, D.J. Myers, E.F. Holby, P. Zelenay, T. Ahmed, Coupling high-throughput experiments and regression

algorithms to optimize PGM-free ORR electrocatalyst synthesis, *ACS Appl. Energy Mater.* 3 (2020) 9083–9088.

[8] J. Park, D.J. Myers, Novel platinum group metal-free catalyst ink deposition system for combinatorial polymer electrolyte fuel cell performance evaluation, *J. Power Sources* 480 (2020), 228801.

[9] A.G. Star, G. Wang, S. Medina, S. Pylypenko, K.C. Neyerlin, Mass transport characterization of platinum group metal-free polymer electrolyte fuel cell electrodes using a differential cell with an integrated electrochemical sensor, *J. Power Sources* 450 (2020), 227655.

[10] G. Wang, L. Osmieri, A.G. Star, J. Pfeilsticker, K.C. Neyerlin, Elucidating the role of ionomer in the performance of platinum group metal-free catalyst layer via *in situ* electrochemical diagnostics, *J. Electrochem. Soc.* 167 (2020), 044519.

[11] M.J. Dzara, K. Artyushkova, M.T. Sougrati, C. Ngo, M.A. Fitzgerald, A. Serov, B. Zulevi, P. Atanassov, Fdr Jaouen, S. Pylypenko, Characterizing complex gas-solid interfaces with *in situ* spectroscopy: oxygen adsorption behavior on Fe-N-C catalysts, *J. Phys. Chem. C* 124 (2020) 16529–16543.

[12] K. Kumar, L. Dubau, M. Mermoux, J. Li, A. Zitolo, J. Nelayah, F. Jaouen, F. Maillard, On the influence of oxygen on the degradation of Fe-N-C catalysts, *Angew. Chem.* 132 (2020) 3261–3269.

[13] E.L. Miller, S.T. Thompson, K. Randolph, Z. Hulvey, N. Rustagi, S. Satyapal, US Department of Energy hydrogen and fuel cell technologies perspectives, *MRS Bull.* 45 (2020) 57–64.

[14] T. Reshetenko, G. Randolph, M. Odgaard, B. Zulevi, A. Serov, A. Kulikovsky, The effect of proton conductivity of Fe-N-C-based cathode on PEM fuel cell performance, *J. Electrochem. Soc.* 167 (2020), 084501.

[15] T. Reshetenko, A. Serov, M. Odgaard, G. Randolph, L. Osmieri, A. Kulikovsky, Electron and proton conductivity of Fe-NC cathodes for PEM fuel cells: a model-based electrochemical impedance spectroscopy measurement, *Electrochim. Commun.* 118 (2020), 106795.

[16] A. Baricci, A. Bisello, A. Serov, M. Odgaard, P. Atanassov, A. Casalegno, Analysis of the effect of catalyst layer thickness on the performance and durability of platinum group metal-free catalysts for polymer electrolyte membrane fuel cells, *Sustain. Energy Fuels* 3 (2019) 3375–3386.

[17] S.T. Thompson, D. Papageorgopoulos, Platinum group metal-free catalysts boost cost competitiveness of fuel cell vehicles, *Nat. Catal.* 2 (2019) 558–561.

[18] C.L. Vecchio, A. Serov, H. Romero, A. Lubers, B. Zulevi, A. Aricò, V. Baglio, Commercial platinum group metal-free cathodic electrocatalysts for highly performed direct methanol fuel cell applications, *J. Power Sources* 437 (2019), 226948.

[19] X. Yang, Y. Wang, G. Zhang, L. Du, L. Yang, M. Markiewicz, J.-y Choi, R. Chenitz, S. Sun, SiO_2 -Fe/N/C catalyst with enhanced mass transport in PEM fuel cells, *Appl. Catal. B: Environ.* 264 (2020), 118523.

[20] D. Wu, C. Peng, C. Yin, H. Tang, Review of system integration and control of proton exchange membrane fuel cells, *Electrochim. Energy Rev.* 3 (2020) 466–505.

[21] J. Lilloja, E. Kibena-Pöldsepp, A. Sarapuu, M. Käärik, J. Kozlova, P. Paiste, A. Kikas, A. Treshchalov, J. Leis, A. Tamm, Transition metal and nitrogen-doped mesoporous carbons as cathode catalysts for anion-exchange membrane fuel cells, *Appl. Catal. B: Environ.* 306 (2022), 121113.

[22] Y. Guo, F. Pan, W. Chen, Z. Ding, D. Yang, B. Li, P. Ming, C. Zhang, The controllable design of catalyst inks to enhance PEMFC performance: a review, *Electrochim. Energy Rev.* 4 (2021) 67–100.

[23] J.-P. Dodelet, V. Glibin, G. Zhang, U.I. Kramm, R. Chenitz, F. Vidal, S. Sun, M. Dubois, Reply to the 'Comment on "Non-PGM electrocatalysts for PEM fuel cells: effect of fluorination on the activity and stability of a highly active NC_{Ar} + NH₃ catalyst"' by Xi Yin, Edward F. Holby and Piotr Zelenay, *Energy Environ. Sci.* 14 (2021) 1034–1041.

[24] X.X. Wang, M.T. Swihart, G. Wu, Achievements, challenges and perspectives on cathode catalysts in proton exchange membrane fuel cells for transportation, *Nat. Catal.* 2 (2019) 578–589.

[25] Y. He, G. Wu, PGM-free oxygen-reduction catalyst development for proton-exchange membrane fuel cells: challenges, solutions, and promises, *Acc. Mater. Res.* 3 (2022) 224–236.

[26] A. Lasia, Electrochemical impedance spectroscopy and its applications. *Modern Aspects of Electrochemistry*, Springer, 2002, pp. 143–248.

[27] B.T.M.E. Orazem, *Electrochemical Impedance Spectroscopy*, 2nd edition, Wiley, New-York, 2017.

[28] D.D. Macdonald, Reflections on the history of electrochemical impedance spectroscopy, *Electrochim. Acta* 51 (2006) 1376–1388.

[29] T. Springer, T. Zawodzinski, M. Wilson, S. Gottesfeld, Characterization of polymer electrolyte fuel cells using AC impedance spectroscopy, *J. Electrochim. Soc.* 143 (1996) 587–599.

[30] M. Eikerling, A. Kornyshev, Electrochemical impedance of the cathode catalyst layer in polymer electrolyte fuel cells, *J. Electroanal. Chem.* 475 (1999) 107–123.

[31] F. Jaouen, G. Lindbergh, Transient techniques for investigating mass-transport limitations in gas diffusion electrodes: I. Modeling the cathode, *J. Electrochim. Soc.* 150 (2003) A1699.

[32] Q. Guo, R.E. White, A steady-state impedance model for a PEMFC cathode, *J. Electrochim. Soc.* 151 (2004), E133.

[33] Y. Bultel, K. Wiezell, F. Jaouen, P. Ozil, G. Lindbergh, Investigation of mass transport in gas diffusion layer at the air cathode of a PEMFC, *Electrochim. Acta* 51 (2005) 474–488.

[34] A. Franco, P. Schott, C. Jallut, B. Maschke, A multi-scale dynamic mechanistic model for the transient analysis of PEFCs, *Fuel Cells* 7 (2007) 99–117.

[35] D. Gerteisen, A. Hakenjos, J.O. Schumacher, AC impedance modelling study on porous electrodes of proton exchange membrane fuel cells using an agglomerate model, *J. Power Sources* 173 (2007) 346–356.

[36] M. Cimenti, D. Bessarabov, M. Tam, J. Stumper, Investigation of proton transport in the catalyst layer of PEM fuel cells by electrochemical impedance spectroscopy, *ECS Trans.* 28 (2010) 147–157.

[37] I. Schneider, M. Bayer, S. Von Dahlen, Locally resolved electrochemical impedance spectroscopy in channel and land areas of a differential polymer electrolyte fuel cell, *J. Electrochim. Soc.* 158 (2011) B343.

[38] J.R. Vang, S.r.J. Andreasen, S.r.K. Kær, A transient fuel cell model to simulate HTPEM fuel cell impedance spectra, in: *Proceedings of the International Conference on Fuel Cell Science, Engineering and Technology*, 2011, pp. 817–30.

[39] J. Mainka, G. Maranzana, A. Thomas, J. Dillet, S. Didierjean, O. Lottin, One-dimensional model of oxygen transport impedance accounting for convection perpendicular to the electrode, *Fuel Cells* 12 (2012) 848–861.

[40] A. Kulikovsky, One-dimensional impedance of the cathode side of a PEM fuel cell: exact analytical solution, *J. Electrochim. Soc.* 162 (2014) F217–F222.

[41] A. Kulikovsky, Exact low-current analytical solution for impedance of the cathode catalyst layer in a PEM fuel cell, *Electrochim. Acta* 147 (2014) 773–777.

[42] A. Baricci, A. Casalegno, A simple analytical approach to simulate the electrochemical impedance response of flooded agglomerates in polymer fuel cells, *Electrochim. Acta* 157 (2015) 324–332.

[43] D. Gerteisen, Impact of inhomogeneous catalyst layer properties on impedance spectra of polymer electrolyte membrane fuel cells, *J. Electrochim. Soc.* 162 (2015) F1431–F1438.

[44] A. Kulikovsky, A simple physics-based equation for low-current impedance of a PEM fuel cell cathode, *Electrochim. Acta* 196 (2016) 231–235.

[45] A. Kulikovsky, A fast low-current model for impedance of a PEM fuel cell cathode at low air stoichiometry, *J. Electrochim. Soc.* 164 (2017) F911–F915.

[46] A. Kulikovsky, Analytical impedance of oxygen transport in a PEM fuel cell channel, *J. Electrochim. Soc.* 166 (2019) F306–F311.

[47] Z. Tang, Q.-A. Huang, Y.-J. Wang, F. Zhang, W. Li, A. Li, L. Zhang, J. Zhang, Recent progress in the use of electrochemical impedance spectroscopy for the measurement, monitoring, diagnosis and optimization of proton exchange membrane fuel cell performance, *J. Power Sources* 468 (2020), 228361.

[48] A. Kulikovsky, O. Shamardina, A model for PEM fuel cell impedance: oxygen flow in the channel triggers spatial and frequency oscillations of the local impedance, *J. Electrochim. Soc.* 162 (2015) F1068–F1077.

[49] T. Reshetenko, A. Kulikovsky, PEM fuel cell characterization by means of the physical model for impedance spectra, *J. Electrochim. Soc.* 162 (2015) F627–F633.

[50] T. Reshetenko, A. Kulikovsky, Impedance spectroscopy characterization of oxygen transport in low- and high-Pt loaded PEM fuel cells, *J. Electrochim. Soc.* 164 (2017) F1633–F1640.

[51] T. Reshetenko, A. Kulikovsky, On the origin of high frequency impedance feature in a PEM fuel cell, *J. Electrochim. Soc.* 166 (2019) F1253–F1257.

[52] T. Reshetenko, A. Serov, A. Kulikovsky, P. Atanassov, Impedance spectroscopy characterization of PEM fuel cells with Fe-NC-based cathodes, *J. Electrochim. Soc.* 166 (2019) F653–F660.

[53] A. Serov, M.H. Robson, M. Smolnik, P. Atanassov, Templated bi-metallic non-PGM catalysts for oxygen reduction, *Electrochim. Acta* 80 (2012) 213–218.

[54] A. Serov, P.B. Atanassov U.S. 9,673,456. "Non-PGM catalysts for ORR based on charge transfer organic complexes", June 6, 2017.

[55] H.T. Chung, D.A. Cullen, D. Higgins, B.T. Sneed, E.F. Holby, K.L. More, P. Zelenay, Direct atomic-level insight into the active sites of a high-performance PGM-free ORR catalyst, *Science* 357 (2017) 479–483.

[56] U. Martinez, S.K. Babu, E.F. Holby, H.T. Chung, X. Yin, P. Zelenay, Progress in the development of Fe-based PGM-free electrocatalysts for the oxygen reduction reaction, *Adv. Mater.* 31 (2019), 1806545.

[57] M.J. Workman, A. Serov, L.K. Tsui, P. Atanassov, K. Artyushkova, Fe-N-C catalyst graphitic layer structure and fuel cell performance, *Acs Energy Lett.* 2 (2017) 1493–1493.

[58] K. Artyushkova, A. Serov, S. Rojas-Carbonell, P. Atanassov, Chemistry of multitudinous active sites for oxygen reduction reaction in transition metal–nitrogen–carbon electrocatalysts, *J. Phys. Chem. C* 119 (2015) 25917–25928.

[59] S. Maldonado, S. Morin, K.J. Stevenson, Structure, composition, and chemical reactivity of carbon nanotubes by selective nitrogen doping, *Carbon* 44 (2006) 1429–1437.

[60] T. Marshall-Roth, N.J. Libretto, A.T. Wrobel, K.J. Anderton, M.L. Pegis, N.D. Ricke, T.V. Voorhis, J.T. Miller, Y. Surendranath, A pyridinic Fe-N₄ macrocycle models the active sites in Fe/N-doped carbon electrocatalysts, *Nat. Commun.* 11 (2020) 1–14.

[61] D. Malko, A. Kucernak, T. Lopes, In situ electrochemical quantification of active sites in Fe-N/C non-precious metal catalysts, *Nat. Commun.* 7 (2016) 1–7.

[62] J. Li, M. Chen, D.A. Cullen, S. Hwang, M. Wang, B. Li, K. Liu, S. Karakalos, M. Lucero, H. Zhang, Atomically dispersed manganese catalysts for oxygen reduction in proton-exchange membrane fuel cells, *Nat. Catal.* 1 (2018) 935–945.

[63] M. Chen, X. Li, F. Yang, B. Li, T. Stracensky, S. Karakalos, S. Mukerjee, Q. Jia, D. Su, G. Wang, Atomically dispersed MnN₄ catalysts via environmentally benign aqueous synthesis for oxygen reduction: mechanistic understanding of activity and stability improvements, *ACS Catal.* 10 (2020) 10523–10534.